

# NANOSCALE REDUCED-GRAPHENE-OXIDE ORIGIN OF SHUNGITE IN LIGHT OF NEUTRON SCATTERING

E. F. Sheka<sup>1</sup>, N. N. Rozhkova<sup>2</sup>, K. Holderna-Natkaniec<sup>3</sup>, I Natkaniec<sup>3,4</sup>

<sup>1</sup>Faculty of Physics, Mathematics and Natural Sciences,  
Peoples' Friendship University of Russia, Moscow, Russia

<sup>2</sup>Institute of Geology, Karelian Research Centre RAS, Petrozavodsk, Russia

<sup>3</sup>Faculty of Physics, Adam Mickiewicz University, Poznan, Poland

<sup>4</sup>Frank Laboratory of Neutron Physics, Joint Institute for Nuclear Research, Dubna, Russia  
sheka@icp.ac.ru, rozhkova@krc.karelia.ru, inat@jinr.ru

**PACS** 61.05.fg, 61.46.+w, 63.22. ±m, 81.05.Uw

New concept of shungite carbon exhibits this raw material as a multi-level fractal structure of nanosize fragments of reduced graphene oxide (rGO) (Int. J. Smart Nano Mat. 1, 1, 2014). The natural rGO deposits turn out to be quite challenging for the current graphene technology. Once consistent with all the block of the available geological and physicochemical data obtained during the last few decades, the concept nonetheless needs a direct confirmation in terms of the current graphene science. The first such acknowledgement has been received just recently when studying photoluminescence (PL) of shungite dispersions (JETP 118, 735, 2014). A close similarity of PL spectra of aqueous dispersion of shungite and those of synthetic graphene quantum dots of the rGO origin has been established. The current paper presents the next direct confirmation provided with neutron scattering. Elastic neutron diffraction and inelastic neutron scattering have left no doubts concerning both graphene-like configuration and chemical composition of basic structural elements of shungite attributing the latter to rGO nanosize sheets with an average  $\sim 6:0.1:2$  (C:O:H) atomic content ratio per one benzenoid unit. The experimental data are supplemented with quantum chemical calculations that allowed suggesting a clear vision of the shungite structure at its first fractal levels.

**Keywords:** shungite; natural nanoscale reduced graphene oxide; multi-stage reduction of graphene oxide; retained water; elastic and inelastic neutron scattering; quantum chemical calculations.

*Received: 13 October 2014*

*Revised: 21 October 2014*

## 1. Introduction

High-yield production of few-layer graphene flakes from graphite is important for the scalable synthesis and industrial application of graphene. Graphene-based sheets show promise for a variety of potential applications, and researchers in many scientific disciplines are interested in these materials. Although many ways of generating single atomic layer carbon sheets have been developed, chemical exfoliation of graphite powders to graphene oxide (GO) sheets followed by deoxygenation to form chemically modified reduced graphene oxide (rGO) has been so far the only promising route for bulk scale production. However, available technologies face a lot of problems among which there are low yield, the potential fire risk of GO and rGO when alkaline salt byproducts are not completely removed, a great tendency to aggregation, a large variety of chemical composition, and so forth (see the latest exhaustive reviews [1, 2] and references therein). In light of this, the existence of natural

rGO is of utmost importance. As if anticipating the future need for the substance, the Nature has taken care of a particular carbon allotrope in the form of well-known shungite mineraloid from deposits of carbon-rich rocks of Karelia (Russia) that strongly kept secret of its origin and rGO-based structure. Just recently has been suggested that shungite carbon has a multilevel fractal structure based on nanoscale rGO sheets [3] that are easy dispersible in water and other polar solvents [4, 5]. Two direct justifications of the suggestion have been obtained. The first one is related to the study of photoluminescence of shungite aqueous and organic dispersions [6, 7] that exhibits properties similar to those of synthetic graphene quantum dots of the rGO origin [8]. The second was obtained in the course of the neutron scattering study that was partially presented in [9] but profoundly discussed in the current paper. The study was initiated by two reasons. The first follows from the leading concept of the suggestion [3] that shungite was born in aqueous environment. Once porous due to its fractal structure, it provides favorable conditions for water confining. Actually, thermal analysis and mass spectroscopy pointed water presence up to a few wt% [10]. As known, the confined water can say much about the space in which it is kept. The other reason concerns a serious problem of detecting chemical composition of rGO, in general, and in shungite, particularly. Usually, the main attention is given to the determination of the C/O ratio focusing primarily of the content of remaining oxygen and leaving the hydrogen content behind brackets [2]. The inelastic neutron scattering (INS) spectroscopy, which is the most hydrogen-sensitive technique, has allowed for the first time not only to detect the small-mass-content hydrogen component of the shungite carbon body but to suggest a general chemical formula for shungite rGO.

## 2. Experimental details

**Neutron experiment.** Neutron scattering study was performed at the high flux pulsed IBR-2 reactor of the Frank Laboratory of Neutron Physics of JINR by using the NERA spectrometer [11]. The investigated samples are illuminated by white neutron beam analyzed by time-of-flight method on the 110 m flight path from the IBR-2 moderator. The inverted-geometry spectrometer NERA allows simultaneous recording of both Neutron Powder Diffraction (NPD) and INS spectra. The latter are registered at final energy of scattered neutrons fixed by beryllium filters and crystal analyzers at  $E_f = 4.65$  meV.

**Samples.** Three powdered shungite samples were subjected to the study. The first pristine shungite Sh1 presents the natural raw material with  $C \geq 95$  wt.% from Shun'ga's deposits [4]. Shungite Sh2 was obtained when drying Sh1 under soft vacuum at temperature  $110^\circ\text{C}$  for a week until the constant weight of the solid is reached. The weight loss, which was attributed to the evaporated water, constitutes 4g per 100g of the solid. The third shungite Sh3 presents a solid condensate of colloids of the shungite Sh1 aqueous dispersions and is produced in the course of the dispersion lengthy drying until the constant weight is reached. Similarly to Sh1, additional heating of Sh3, sustained under ambient conditions for a long time, at soft vacuum and temperature above  $100^\circ\text{C}$  results in its releasing from the retained water constituting  $\sim 4\%$  of the total mass. Raman scattering [3], high-resolution solid state  $^{13}\text{C}$  NMR [10], and Auger spectroscopy [5] show a deep similarity of shungites Sh1 and Sh3. Powdered spectral graphite was used to register both the reference NPD and INS spectrum from pure carbon material.

## 3. Neutron powder diffraction

A set of NPD plottings for the three shungite samples at 20 K is presented in Fig. 1. The data are related to samples in aluminum sample holder and cryostat due to which the

plottings are overloaded with Al(hkl) reflections. Exempted from the Al reflections and corrected for background inelastic scattering, NDP plottings of Sh1 and Sh2 are presented in Fig. 2. Similarly to the reference graphite spectrum, given at the bottom, the main features of the shungite diffractograms concern peaks related to Gr(002), Gr(100) and Gr(110) reflections all of which are broadened and upshifted. Figure 3 presents a detailed view on Gr(002) peaks. As seen in the figure, the narrow peak of graphite, the shape and width of which correspond to the resolution function of spectrometer and whose position determines  $d_{002}$  interplanar spacing between the neighboring graphite layers, is substituted with broad peaks whose characteristics are given in Table 1. To fix the positions  $A_{002}$  of the peaks maxima and to obtain the relevant FWHMs,  $B_{002}$ , the Gauss fitting procedure was applied. According to the fitting,  $A_{002}$  and  $B_{002}$  values of all shungite samples are identical within the limits of standard errors.

TABLE 1. Characteristics of Gr(002) peaks

Samples	Peak position, $A_{002}$ , Å	FWHM, $B_{002}$ , Å
Graphite	$3.3501 \pm 0.0002$	$0.0341 \pm 0.0006$
Sh1	$3.4513 \pm 0.0015$	$0.5408 \pm 0.0063$
Sh2		
Sh3		

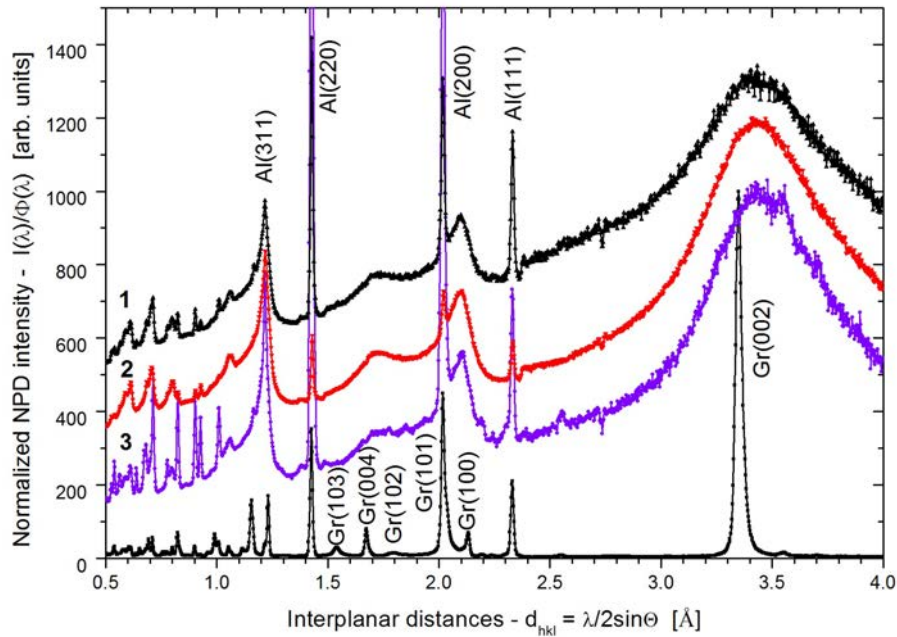


FIG. 1. NPD of spectral graphite (Gr) and shungites Sh1 (1), Sh2 (2), and Sh3 (3) recorded at  $T=20$  K. Scattering angle  $2\Theta = 117.4^\circ$ . The data are normalized per neutron flux intensity  $\Phi(\lambda)$  at each neutron wave length  $\lambda$ ; Gr(hkl) and Al(hkl) denote characteristic diffraction peaks of spectral graphite and cryostat aluminum at different Miller indexes, respectively

Slight upshift of the shungite peaks convincingly evidences a conservation of the graphite-like structure of all the samples, while the peak wide broadening tells about a

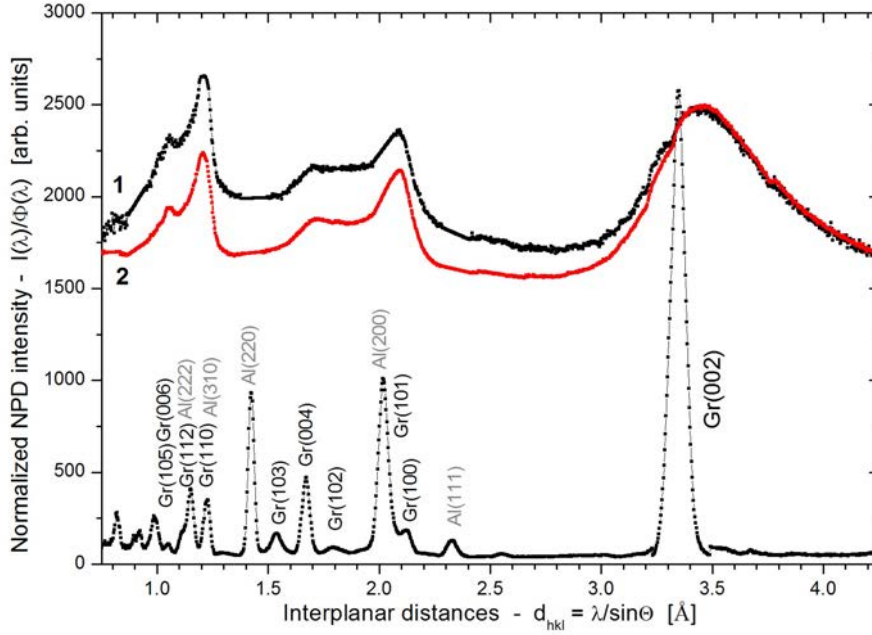


FIG. 2. NPD of shungites Sh1 (1) and Sh2 (2) recorded at  $T=20$  K after extraction of Al(hkl) reflections. Scattering angle  $2\Theta = 44.7^\circ$ . The data are normalized per neutron flux intensity  $\Phi(\lambda)$  at each neutron wave length  $\lambda$ ; Gr(hkl) (black) and Al(hkl) (gray) denote characteristic diffraction peaks of spectral graphite and cryostat (alongside with sample holder) aluminum at different Miller indexes, respectively

considerable space restriction. The latter is usually attributed to the narrowing of the coherent scattering region (CSR) of scatterers. According to widely used Scherrer's equation, the FWHM of a diffraction peak  $B$  and the CSR length  $L_{CSR}$  are inversely connected:  $B = k\lambda/L_{CSR} \sin \Theta$ , where  $k$  is a fitting factor,  $\lambda$  and  $\Theta$  are the neutron wave length and scattering angle. When the diffraction study is performed for a set of samples under the same conditions, it is possible to take one of the samples as the reference and to determine  $L_{CSR}$  of the remaining samples addressing to that of the reference. In our study,  $L_{CSR}^{ref}$  is attributed to crystalline graphite and constitutes  $\sim 20$  nm along  $c$  direction [12]. Therefore,  $L_{CSR}^c$  of the studied shungites can be determined as

$$L_{CSR}^c = (B_{002ref}/B_{002}) (\lambda/\lambda_{ref}) L_{CSR}^{ref}. \quad (1)$$

Substituting  $\lambda/\lambda_{ref}$  by the ratio of the Gr(002) peak positions  $A_{002}/A_{002ref}$  and using  $B_{002}$  values given in Table 1, we obtain  $L_{CSR}^c = 1.3$  nm. The data correlates well with those of 2.18 nm and 2.30 nm for Sh1 and Sh3, respectively, obtained by X-Ray diffraction [13]. Summarizing NPD and X-Ray data,  $L_{CSR}^c$  of  $\sim 1.5$ –2 nm can be suggested. The obtained  $L_{CSR}^c$  corresponds to the coherency along the direction normal to graphene layers and points to  $\sim 5$ –6 layer structure of the relevant stacks. It should be noted that a multi-layer graphene-like packing is characteristic for rGO of any origin [1].

As early pointed [14],  $L_{CSR}^a$ , which determines the layer lateral dimension, is characterized by the width of Gr(110) peak. On the basis of the Scherrer equation and using

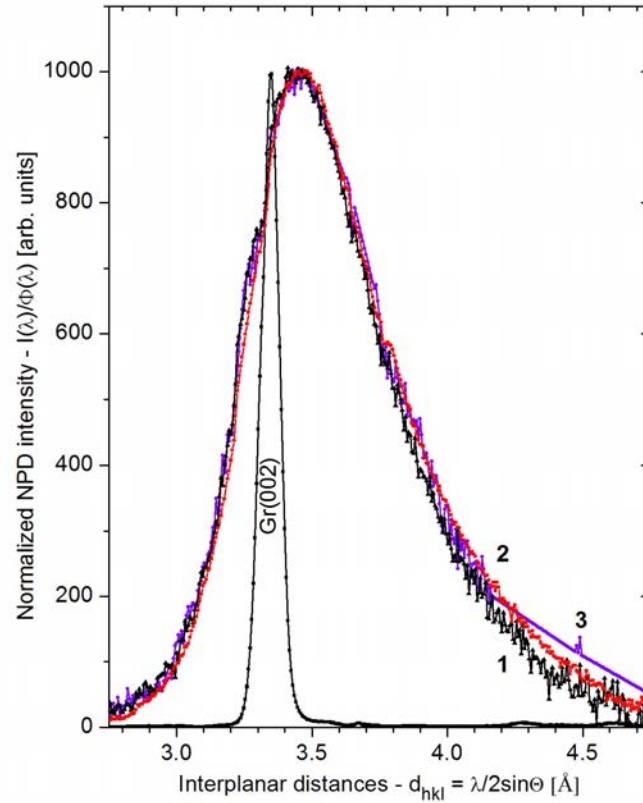


FIG. 3. NDP fragments of spectral graphite (Gr) and shungites Sh1 (1), Sh2 (2), and Sh3 (3) in the region of Gr(002) diffraction peaks;  $T=20$  K; scattering angle  $2\Theta = 44.7^\circ$ . The data are normalized per neutron flux intensity  $\Phi(\lambda)$  at each wave length of incident neutrons  $\lambda$ ; after a linear background subtraction, the intensity maxima of all the peaks are normalized to 1000 arbitrary units

results presented in Fig.2, the corresponding value can be evaluated following the ratio

$$L_{CSR}^a = L_{CSR}^c \frac{A_{110} \cdot B_{002}}{A_{002} \cdot B_{110}} \quad (2)$$

$B_{110}$  values of the Gr(110) peak of both shungites are quite similar and constitute  $\sim 0.0723 \text{ \AA}$  so that the relevant  $L_{CSR}^a \approx 1.93 L_{CSR}^c$ . As known,  $\{hk0\}$  reflections are influenced by not only the lateral extent of the graphene layers but the presence of both translational and rotational disorder (turbostratic structure) of the stacks [14]. Therefore, the obtained  $L_{CSR}^a \sim 3\text{--}4 \text{ nm}$  can be considered as the upper limit of the lateral size of graphene sheets while the size of individual rGO sheets might be significantly less.

#### 4. Inelastic neutron scattering

Figure 4 presents time-of-flight (TOF) INS spectra of the studied samples at  $T=20\text{K}$ . The spectra are summarized over 15 scattering angles, normalized per 10 hours exposition time. As seen in the figure, the INS intensity from graphite is at the level of the instrumental background and can be taken as the background to be extracted from the shungite spectra for both experimental background and INS from carbon atoms to be excluded. The spectra clearly exhibit strong scattering from all the samples in contrast with that from graphite

thus indicating that all of them are evidently hydrogen-enriched. At the same time, the spectra differ by both intensity and shape. Thus, if the spectra of Sh1 and Sh3 differ only in intensity, the spectra of Sh1 and Sh2 differ in shape as well. The first finding points that the hydrogen atom dynamics in Sh1 and Sh3 is rather identical while in Sh2 the later is quite different. As shown in [9], the difference TOF spectrum 1–2 between spectra 1 and 2 evidently presents the spectrum of the released water since Sh2 was produced from Sh1 by lengthy heating, which was followed by removing water previously retained in Sh1. At the same time, the spectrum of Sh2 is quite intense, which undoubtedly points to the presence of hydrogen atoms incorporated in the carbon structure of shungite. Therefore, the observed INS spectra of shungites are provided with incoherent inelastic neutron scattering (IINS) from hydrogens incorporated in the shungites structure and contained in the retained water.

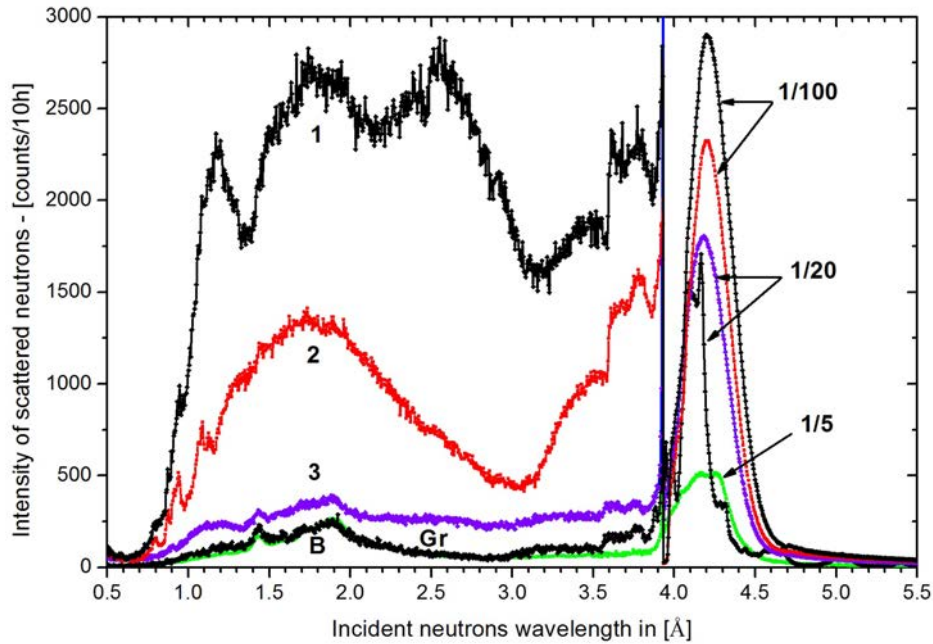


FIG. 4. Time-of-flight INS spectra from shungites Sh1 (1=100g), Sh2 (2=96g), Sh3 (3=10g) and spectral graphite (Gr=10g). Curve B presents background from Al cryostat and sample holder material.  $T=20\text{K}$ . The intensity of elastic peaks is 100-fold, 20-fold, and 5-fold reduced for Sh1 and Sh2, Sh3 and graphite, and background, respectively. Spectra are normalized per 10 hours exposition time at constant power of the IBR-2 equal 1.9 MW

Within the confines of commonly used incoherent inelastic one-phonon scattering approximation, the IINS spectra intensity is determined by the scattering cross-section (see for example Ref. 15) as

$$\sigma_1^{inc}(E_i, E_f, \varphi, T) \approx \sqrt{\frac{E_f}{E_i}} \frac{\hbar |Q(E_i, E_f, \varphi)|^2}{\omega} \sum_n \frac{(b_n^{inc})^2}{M_n} \frac{\exp(-2W_n)}{1 - \exp\left(-\frac{\hbar\omega}{k_B T}\right)} G_n(\omega) \quad (3)$$

Here,  $Q(E_i, E_f, \varphi)$  is the neutron momentum transfer;  $\omega = (E_i - E_f)$  is the neutron energy transfer;  $b_n^{inc}$  and  $M_n$  are the incoherent scattering length and mass of the  $n$ -th atom;  $\exp(-2W_n)$  is the Debye-Waller factor;  $G_n(\omega)$  presents the  $n$ -th atom contribution into the

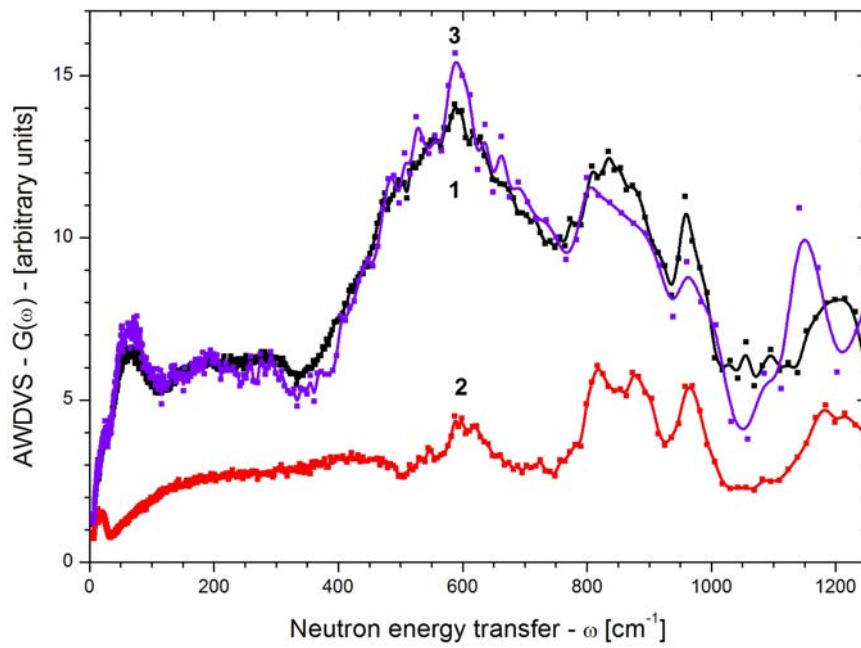


FIG. 5. One-phonon AWDVS spectra of shungites Sh1 (1), Sh2 (2), and Sh3 (3) at 20K

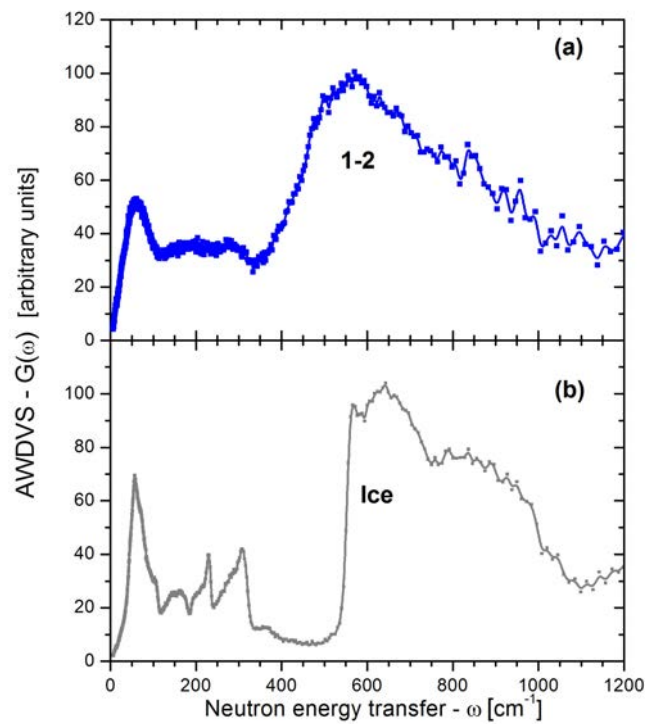


FIG. 6. (a) The difference spectrum 1-2 attributed to retained water; (b)  $G(\omega)$  spectrum of  $I_h$  ice.  $T = 20K$

amplitude-weighted density of vibrational states (AWDVS) expressed as

$$G(\omega) = \sum_n G_n(\omega) = \sum_n \sum_j [A_j^n(\omega)]^2 \delta(\omega - \omega_j). \quad (4)$$

Here,  $A_j^n(\omega)$  is the  $n$ -th atom contribution into the eigenvector of the  $j$ -th phonon mode thus presenting the amplitude of the  $n$ -th atom displacement at the vibrational frequency  $\omega_j$ .

Figure 5 presents one-phonon AWDVS  $G(\omega)$  spectra obtained in the course of a standard treatment procedure [15] and related to the TOF spectra shown in Fig. 4 after extraction of the INS spectrum of graphite taken as background and normalization of the TOF spectra per  $10^6$  monitor counts of incident neutrons. When obtaining  $G(\omega)$  spectra, Debye-Waller factors were taken as unity due to low temperature and rather narrow frequency region. The spectra were not corrected on multi-phonon contribution that is quite small at low temperature. All the spectra are normalized per 10 g of mass. As seen in the figure,  $G(\omega)$  spectra of Sh1 and Sh3 are practically identical. Changing in the fine structure of spectrum 3 above  $500 \text{ cm}^{-1}$  may be connected with either poor statistic of experimental data due to small mass of shungite Sh3 or reconstruction of its structure in the course of transformation of the pristine shungite Sh1 to Sh3 first through dispersion in water and then consolidation of a solid phase after the water evaporation.  $G(\omega)$  spectrum of Sh2 differs from the above two spectra quite significantly. The difference between  $G(\omega)$  spectra 1 and 2 is presented in Fig. 6a as spectrum 1–2.

Analyzing the spectra obtained, three features can be noted. The first concerns spectrum 1–2 in Fig. 6a that can be evidently considered as the spectrum  $G^{wat}(\omega)$  of retained water. Actually, the spectrum has much in common with that of bulk water presented in Fig. 6b and presents the contribution of 4wt% water in the spectrum of the pristine shungite Sh1. It is pretty similar to those well known for retained water in silica gels [16, 17], Gelsil glasses [18], nanosized graphite oxide [19], and various zeolites [20]. The second feature is related to spectrum 2 in Fig. 5 that evidently exhibits hydrogen atoms in the shungite core not connected with water. The relevant  $G^{core}(\omega)$  differs drastically from the water one and has much in common with that one of a synthetic rGO [21] thus confirming the rGO nature of shungite. The spectrum is characterized by a considerable flattening up to  $500 \text{ cm}^{-1}$  and reveals a pronounced structure in the region of  $600$ – $1200 \text{ cm}^{-1}$ . The third feature concerns the evident absence of the retained water crystallization so that the  $G^{wat}(\omega)$  spectrum represents bound water [19]. As shown in [22], this water may be supercooled without crystallization up to very low temperature.

As known, water molecules can be retained either on the surface of solid nanoparticles (see adsorbed water on aerosil [17]) and in the interfacial region of layered nanostructures [19] or in pores formed by different bodies [18, 20]. The multi-layer stack structure of shungites with interplanar spacing of  $\sim 3.5 \text{ \AA}$  leaves no possibility of introducing  $1.75 \text{ \AA}$ -thick water molecules between the layers. The latter can be accommodated either on the outer surface of  $\sim 1.5$ – $2 \text{ nm}$  shungite stacks or in pores made of the latter and their aggregates. Small angle neutron scattering (SANS) from shungite [23] exhibited pores of  $2$ – $10 \text{ nm}$  and  $> 20 \text{ nm}$  in size thus pointing the place of the water accommodation. This explains a very deep similarity that is observed between the AWDVS spectra of the water retained in pores of silica gels [16, 17], Gelsil glass [16] and  $G^{wat}(\omega)$  spectrum of shungite.

## 5. rGO sheet modeling

The hydrogen-enriched rGO core is the main intrigue of the current study. According to [24], the remaining chemical addends are concentrated in the circumference of graphene sheets and are mainly presented by carbonyl units complemented by a small portion of hydroxyls. However, in the case of shungite [3], the relevant oxygen contribution is too high which contradicts with real data indicating a small amount of oxygen at the level of 3–2 wt% as shown by the latest point microanalysis that accompanies extensive HRTEM study [25]. Moreover, as follows from the  $G^{core}(\omega)$  spectrum in Fig. 5, there is no indication of the presence of bands, which could be attributed to hydroxyls (either in the region of 90–100  $cm^{-1}$ , which is characteristic for hydroxyls attached to silica [17], or at 400–500  $cm^{-1}$ , which is typical for hydroxyls on carbon substrate [21, 26]). In contrast, clearly vivid maxima at  $\sim 610$   $cm^{-1}$ , 820  $cm^{-1}$ , 880  $cm^{-1}$ , 960  $cm^{-1}$ , and 1200  $cm^{-1}$ , which fall in the region of the most characteristic non-planar deformational vibrations of the alkene C–H bonds [21, 26], are observed. The hydrogen presence is supported by the hydrophobicity of rGOs that is often noted by chemists. The finding convincingly points to the presence of C–H bonds in the circumference of rGO nanosheets thus exhibiting a *post factum* hydrogenation of the pristine rGO that is produced in the course of deoxygenating the pristine GO [3].

TABLE 2. Chemical composition and mass content of differently reduced (5, 5) rGOs in vacuum

Atomic composition	Mass content, wt %			Remarks
	C	O	H	
$C_{66}O_{22}H_2$	69.13	30.70	0.17	calc., Fig. 7b
$C_{66}O_9H_{13}$	83.46	15.17	1.37	calc., Fig. 7d
$C_{66}O_6H_{16}$	87.61	10.62	1.77	calc.
$C_{66}O_5H_{17}$	89.09	9.00	1.91	calc.
$C_{66}O_4H_{18}$	90.62	7.32	2.06	calc.
$C_{66}O_3H_{19}$	92.20	5.59	2.21	calc., Fig. 7e
$C_{66}O_2H_{20}$	93.84	3.79	2.37	calc.
$C_{66}O_1H_{21}$	95.54	1.93	2.53	calc. Fig. 9a
$C_{66}H_{22}$	97.30	-	2.70	calc.
Product 1 $C_{66}O_6H_{16}^*$ $(C_6O_{0.54}H_{1.45})^{**}$	$85.7 \pm 1.0$	$9.59 \pm 0.5$	$1.06 \pm 0.5$	Exp. [30]
Product 2 $C_{66}O_3H_{19}^*$ $(C_6O_{0.27}H_{1.73})^{**}$	$92.0 \pm 1.0$	$5.5 \pm 0.5$	$1.5 \pm 0.5$	Exp. [29]
Shungite $C_{66}O_2H_{20}^*$ $(C_6O_{0.18}H_{1.82})^{**}$	95.3-92.4***	3.3-2.5***		Exp. [25]

\*Proposed (5, 5) rGO compositions that best fit experimental data.

\*\*Averaged atomic composition per one benzenoid unit.

\*\*\*The scatter in the data obtained from measurements in four points of one sample.

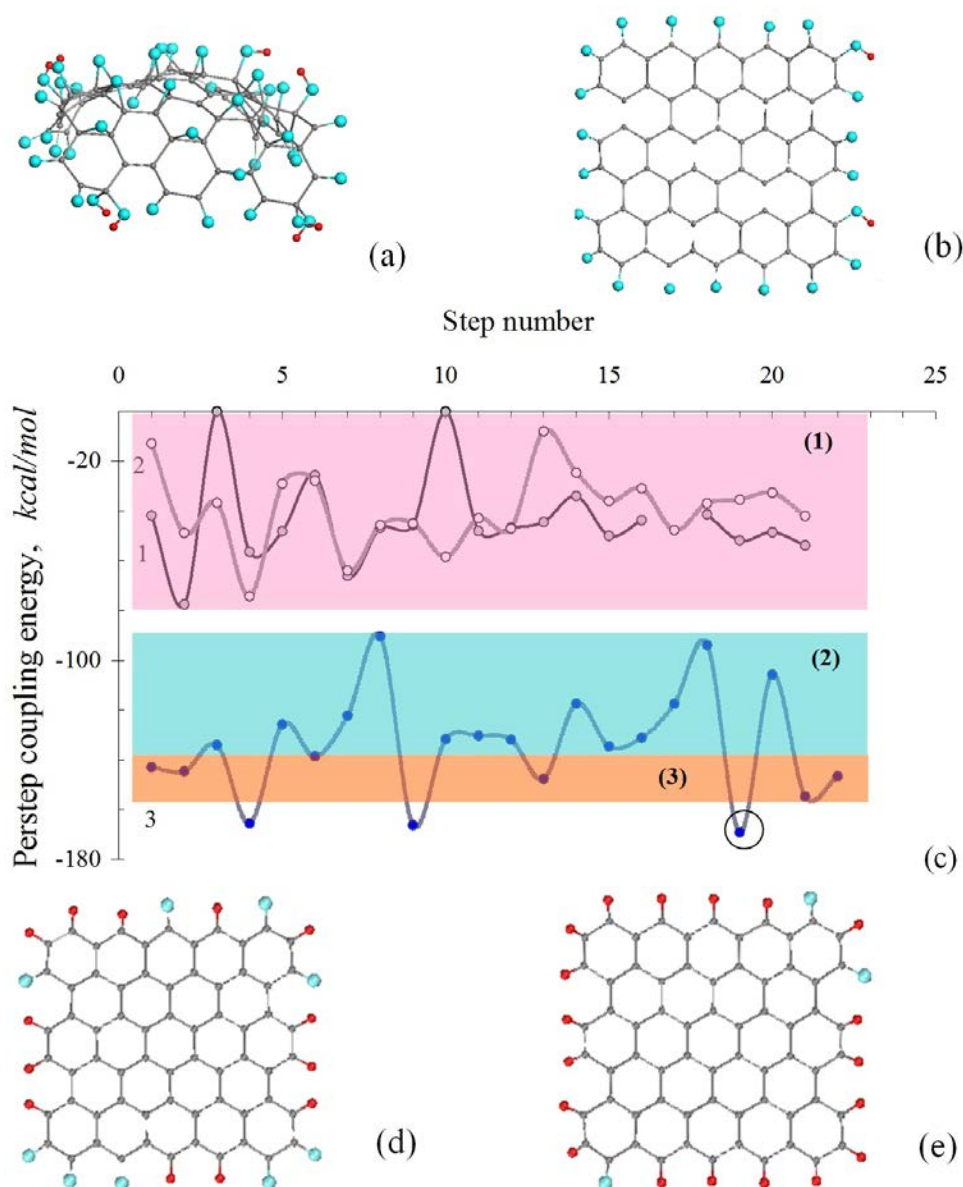


FIG. 7. (a). Equilibrium structure of  $\sim 1$  nm (5, 5) GO sheet corresponding to one-side oxidation of the pristine (5, 5) NGr molecule [24]. (b). Model rGO sheet corresponding to the first stage of the (5, 5) GO deoxygenating that affects the atoms in the basal plane of the GO sheet only (zone 1, soft reduction) [24]. (c). *per step* coupling energies related to the one-side oxygenation of the (5, 5) NGr molecule: O- and OH-attachments to the basal plane (curves 1 and 2, respectively) and the combination of O and OH attachments in the circumference (curve 3) [24]; the circled point corresponds to the formation of carbonyl unit on the rGO circumference with the largest coupling energy. (d) and (e) Model (5, 5) rGO sheets corresponding to a medium and hard reduction of the (5, 5) GO in the framework of zone 2 and zone 2 and 3 in (c), respectively. Small gray and black balls present carbon and hydrogen atoms while big gray balls mark oxygen atoms

Usually, rGO structural models are tightly connected with those of GO ones thus relating to the latter when removing all oxygen containing units from the sheet basal plane.

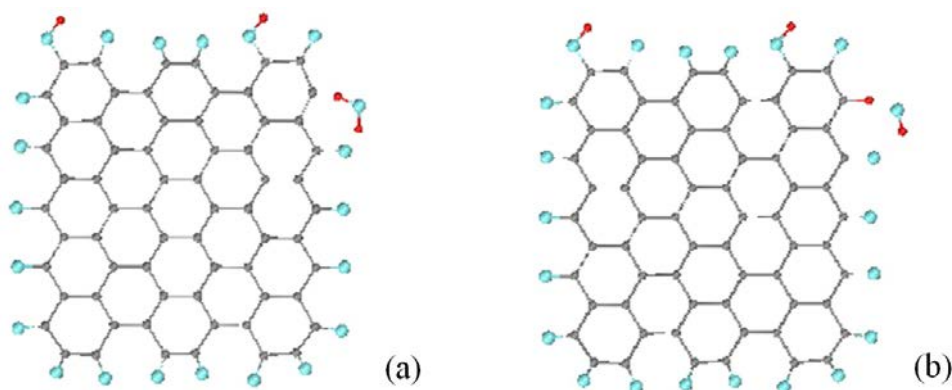


FIG. 8. a. Starting configuration of the complex of one water molecule and the soft-reduced (5, 5) rGO molecule after removing one oxygen atom in the circumference. (b). Equilibrium structure of the (5, 5) rGO + water complex (UHF calculations). The atom marking see in the caption to Fig.7

There is a large variety of GO models, mainly just ‘drawn’ basing on a chemical intuition. On this background, there is a definite preference of that one produced in due course of a sequential polyderivatization of a graphene flake [24] in the framework of the computational experiment subordinated to a particular algorithm [27]. Thus constructed (5, 5) GO molecule is shown in Fig. 7a. The latter was computationally synthesized in the course of the stepwise oxidation of the pristine (5, 5) nanographene (NGr) molecule (a rectangular graphene fragment containing  $n_a=5$  and  $n_z=5$  benzenoid units along armchair and zigzag edges, respectively) in the presence of three oxidants, such as O, OH, and COOH [24].

The GO reduction concerns removing oxygen containing units. As evidences by the *per step* coupling energies, which accompany the attachment of the oxidants to either basal plane atoms (curves 1 and 2 in Fig. 7c) or edge atoms in the circumference area (curve 3), the reduction is obviously multistage or multimode one. Actually, the oxygen atoms located at the basal plane of the pristine (5, 5) GO molecule (within zone 1) should be removed first. The corresponding (5, 5) rGO molecule is shown in Fig. 7b. This apparently happens at the first stage of the real reduction and may present the final state of the reduction procedure when the latter is either short-time or not very efficient; the relevant reduction might be attributed to a soft one. The corresponding mass content of the obtained rGO molecule is given in Table 2. These and other calculated data in the table are related to the relevant rGO molecules in vacuum.

However, when the reduction occurs during long time or under action of strong reducing agents, it may concern oxidants located at the rGO molecules circumference. Such two-step reduction of a pristine GO has been actually fixed [28]. However, due to a waving character of the *per step* coupling energy dependence with a large amplitude from  $-90$  kcal/mol to  $-170$  kcal/mol, the second step reduction could be highly variable. Thus, limiting the energy interval to 30 kcal/mol (removing oxidants covered by zone 2) results in remaining only 9 oxygen atoms (see Fig. 7d) instead of 22 in the pristine (5, 5) rGO sheet shown in Fig.7b. As seen in Table 2, such a reduction halves the oxygen content and causes the appearance of a remarkable quantity of hydrogen. Further strengthening of the reduction, counted by lowering the number of remaining oxygen atoms, gradually decreases the oxygen content while increasing the hydrogen contribution. Consequently, the structures presented in Figs. 7b, 7d, and 7e might be attributed to rGOs obtained in the course of soft, medium, and hard reduction, respectively.

Coming back to the rGO hydrogenation, we face the problem, whence comes the hydrogen. As discussed in [3], the hydrogenation of the pristine graphene lamellae loses to oxidation on all parameters in the course of the first stage of the graphenization of carbon rich sediments. Therefore, GO sheets similar to that shown in Fig. 7a do not contain either mono-atomic or diatomic hydrogen among its framing atoms. However, the abundance of hot water around GO and rGO sheets, which accompanies the shungite derivation, suggests that water can provide not only the GO reduction (see the corresponding discussion in [3]), but the hydrogenation of the formed rGO as well. Actually, the release of one of the edge carbon atoms of the rGO within zone 1 shown in Fig. 7c from oxygen makes the atom highly chemically active [27] and promotes the dissociation of a water molecule in the vicinity of this atom and neighboring oxygen. A possibility of such reaction is demonstrated in Fig. 8. The water molecule, initially located at 1.10 Å apart from both the carbon and oxygen atoms in Fig. 8a, willingly dissociates (see Fig. 8b) while the formed hydroxyl remains in the vicinity of the newly formed C-H bond, once connected with both the bond hydrogen atom and neighboring oxygen via hydrogen bonds. The energy gain of the reaction constitutes 25.94 kcal/mol which points to its high efficacy. Evidently, the considered mechanism of the rGO hydrogenation, parallel or alongside with the simultaneous GO reduction, might not be the only one and will strongly depend on the reducing agents such as, for example, alcohols under critical regime [29]. Actually, hydrophobic character of produced rGOs, oppositely to high hydrophilicity of the pristine GO, which is noted by many chemists, strongly evidences the reality of the hydrogenation of pristine rGOs.

When supposing that in due course of the *post factum* hydrogenation of the rGO molecule each of the remaining oxygen atoms is substituted by one hydrogen, the limiting case, presented by C<sub>66</sub>H<sub>22</sub> polyhydride in Table 2, corresponds to the one-atom-hydrogen termination of the edge atoms of the (5, 5) NGr sheet. However, as shown in [31], in this case, the edge atoms remain yet still chemically active and are able to accept one more hydrogen atom each. The addition of the second hydrogen atom in response to removing one oxygen atom can occur at any stage of the hydrogenation of the circumference area. However, this action influences the oxygen content only slightly due to which the data presented in Table 2 may be used for estimation of the C/O ratio. In contrast, the hydrogen content may considerably increase thus greatly lifting, for example, the IINS intensity, which should be taken into account when analyzing IINS spectra.

## 6. Chemical composition of rGOs: Comparison with experiment

The dependence of the chemical composition of final products of the GO reduction on the efficacy of the *post factum* hydrogenation results in the formation of a large class of oxyhydrides of graphene that all are covered under the term rGO. This explains the C/O variation characteristic for rGOs of different origin, a large scale of which is observed in practice depending on which namely chemicals and how long the latter are involved in the reduction procedure [2]. A common situation is presented in Table 2 by two extended accounts related to synthetic rGO [29, 30]. As seen from the table, the mass content of the two products is well consistent with that of C<sub>66</sub>O<sub>6</sub>H<sub>16</sub> and C<sub>66</sub>O<sub>3</sub>H<sub>19</sub> atomic compositions, the former of which tells about uncompleted (medium) reduction of the rGO circumference area of product 1 while the latter evidences quite hard reduction in the case of product 2. The relevant (5, 5) rGO molecule is shown in Fig. 7e. As for shungite, its formation during a long period of time allows for suggesting a hard type of the reduction, which explains low oxygen content in the carbon-most-rich shungite deposits [25] and simultaneously provides a high stability of the chemical composition of the rGO basic elements. The relevant C/O

mass content given in Table 2 was determined by point microanalysis in different areas of shungite samples when performing an extensive HRTEM study. According to the data, the chemical composition of shungite is in between  $C_{66}O_2H_{20}$  and  $C_{66}O_1H_{21}$  compositions, closer to the former.

TABLE 3. Chemical composition and mass content of reduced (5, 5) rGO of the  $C_{66}O_1H_{21}$  chemical composition in the presence of retained water

Atomic composition	Mass content, wt %			Remarks
	C	O	H	
$C_{66}O_1H_{21}$ ( $C_6O_{0.09}H_{1.91}$ )*	95.54	1.93	2.53	calc.
$C_{66}O_1H_{21} + 2H_2O$	91.56	5.55	2.89	calc.
Shungite	96.52–92.52	4.22–2.43		Exp. [25]

\*Averaged atomic composition per one benzenoid unit.

The above analysis concerned rGO models in vacuum while the current study has revealed 4wt% water in shungite sustained under ambient conditions. The water content corresponds to 34 a.u. and 35 a.u. with respect to the total mass of the above two compositions, respectively, which points to the presence of two water molecule per each (5, 5) rGO sheet resulting in replacing the previous compositions by  $C_{66}O_4H_{24}$  and  $C_{66}O_3H_{25}$ . Assuming that the composition mass content must be consistent with empirical data for shungite and basing on the C/O regulation presented in Table 2, the preference should be given to the latter one in contrast to the former that provides too high oxygen content. Table 3 presents the mass content redistribution caused by retained water. As seen in the table, new data are quite consistent with experimental thus allowing to lay the  $C_{66}O_1H_{21}$  composition of the (5, 5) rGO sheet into the ground of a reliable model for shungite structure.

## 7. Basic elements of shungite fractal structure

Taking  $\sim 1$  nm (5, 5) rGO sheet of  $C_{66}O_1H_{21}$  atomic composition as the model basic element of shungite as well as four-six-layer stacks of the element (see the top part of Fig. 9), is possible to suggest a microscopic vision of the shungite at the third level of its fractal structure concerning individual globules. Irregular structures of the stacks in Fig.9 reflect a possible presence of both translational and rotational disorder (turbostratic structure) of the latter [14]. Presented in Fig. 10 is a planar projection of a globe structure voluntary packed with differently projected stacks of different size. The interglobe pores are compatible with linear dimensions of rGO stacks and are quite suitable for retaining water. As for retained water, it is well known that in the low-frequency region ( $0-1000$   $cm^{-1}$ ), the IINS spectrum of bulk water  $G^{ice}(\omega)$  shows a hindered translational spectrum (I and II in Fig. 6b) alongside with the low-frequency Debye phonon-like acoustical contribution and a librational spectrum (III). Both the hindered translational and rotational (librations) modes are present in water because of intermolecular hydrogen bonds (HB) that are formed by each water molecule surrounded by other four ones. The configuration changes when water molecules can not move freely in space due to which it is quite natural to expect a strong spectral modification when passing from the bulk to retained water, which is clearly seen in Fig. 6a. Actually, the only ice mode positioned at  $\sim 56$   $cm^{-1}$  (HB bending) is retained in the  $G^{wat}(\omega)$  spectrum while  $\sim 150$   $cm^{-1}$  (HB bending) as well as  $\sim 224$  and  $\sim 296$   $cm^{-1}$  (HB stretchings)

ice modes reveal clearly seen flattening and downshift. Analogous spectral modification takes place with respect to the ice librational modes forming a broad band in the region of  $600\text{--}1200\text{ cm}^{-1}$ . The band is provided with water molecule rotations around three symmetry axes whose partial contribution determines the band shape. As shown by detail studies [18, 20], the modes conserve their dominant role in the IINS spectra of retained water, albeit are downshifted, when water molecules are coupled with the pore inner surface via hydrogen bonds. This very behavior is characteristic for the  $G^{wat}(\omega)$  spectrum in Fig. 6a. The three-ax partial contribution is sensitive to both chemical composition of the pore walls and the pore size [20]. Thus, the downshift of the red edge of the band from  $550\text{ cm}^{-1}$  to  $320\text{ cm}^{-1}$  when going from the  $G^{ice}(\omega)$  spectrum to the  $G^{wat}(\omega)$  one highlights the shungite pore size of a few  $nm$ , which is well consistent with SANS data [23].

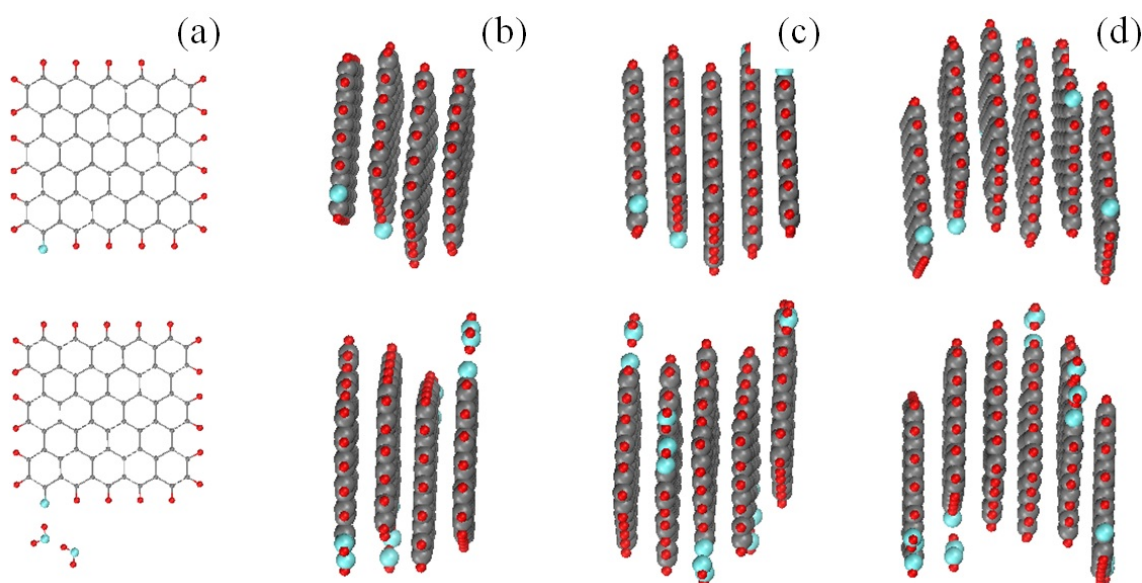


FIG. 9. (a). Equilibrium structure of  $\sim 1\text{ nm}$  (5, 5) rGO sheets of the  $C_{66}O_1H_{21}$  chemical composition, ‘dry’ (top) and ‘wet’ (bottom), respectively. (b)–(d). Arbitrary models of four-, five-, and six-layer stacks of the relevant rGO sheets with  $3,5\text{\AA}$  interlayer distance. Big and small dark gray balls mark carbon and hydrogen atoms when white balls do the same for oxygen

As was mentioned earlier, 4 wt% water in Sh1 implies two water molecules per one rGO sheet of the  $C_{66}O_1H_{21}$  chemical composition. The two molecules are evidently located in the vicinity of the only oxygen atom in the sheet circumference, once connected with both the atom and between each other by hydrogen bonds (see the bottom of Fig. 9). Analogously to ‘dry’ sheets, the ‘wet’ ones are grouped in graphite-like stacks that form globules when aggregating. A possible model of such a globe is shown in Fig. 11. As seen in the figure, the stacks with water molecules can be comfortably packed forming pores of a comparable size. The stacks surface forms the inner surface of the pores that are carpeted with hydrogens while the only oxygen atom is shaded by two water molecules. The amount of oxygen atoms determines the quantity of water which is bound with the pore surface thus considerably limiting the monolayer coverage of the pores at much lower level than that revealed by the IINS study of graphite oxide [19].

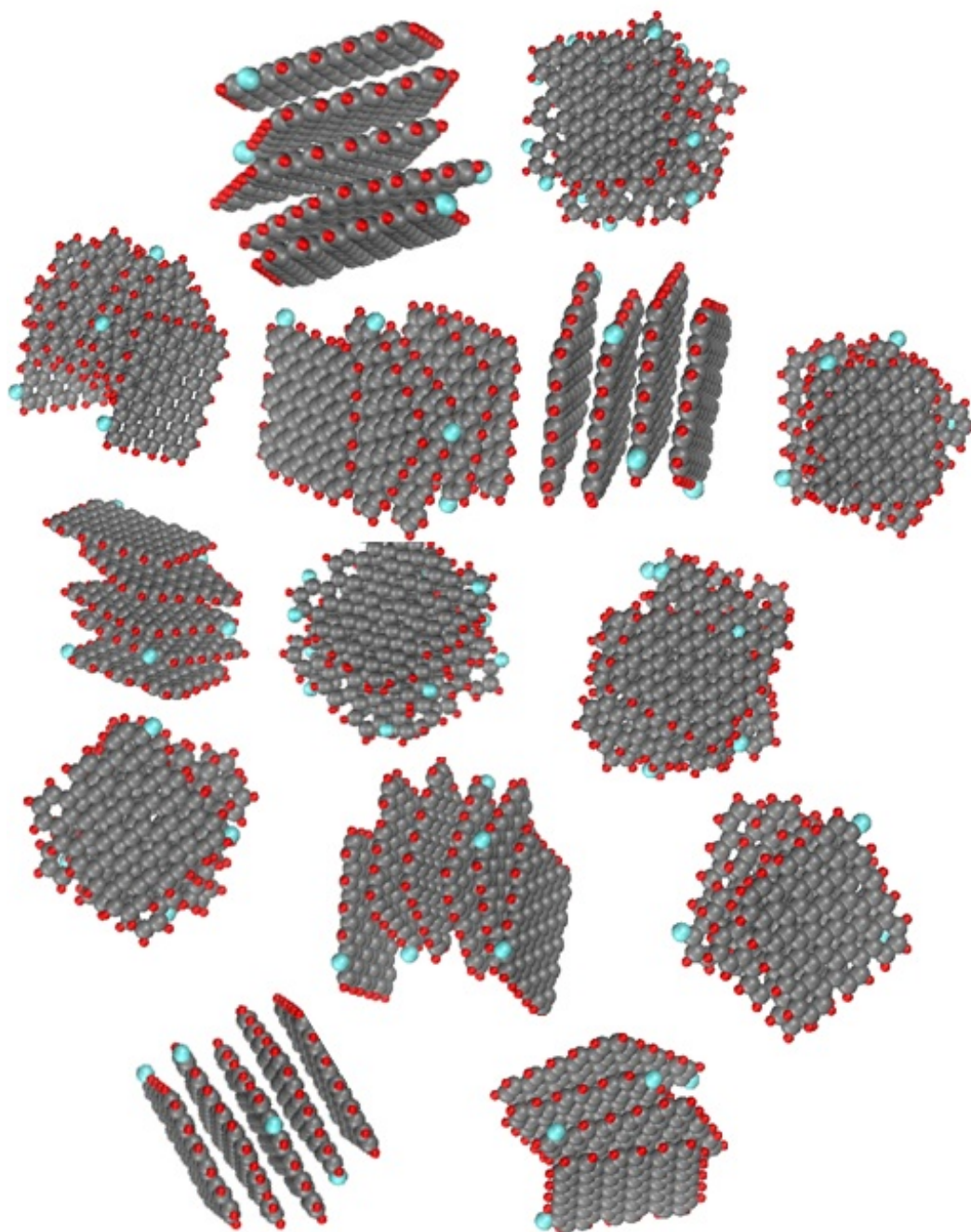


FIG. 10. Planar presentation of a model of 'dry' shungite globule consisting of a set of four-, five- and six-layer stacks of 'dry' (5, 5) rGO sheets of the  $C_{66}O_1H_{21}$  chemical composition voluntarily located and oriented in space. Linear dimensions along the vertical and horizontal are of  $\sim 6$  nm. The atom marking see in the caption to Fig.9

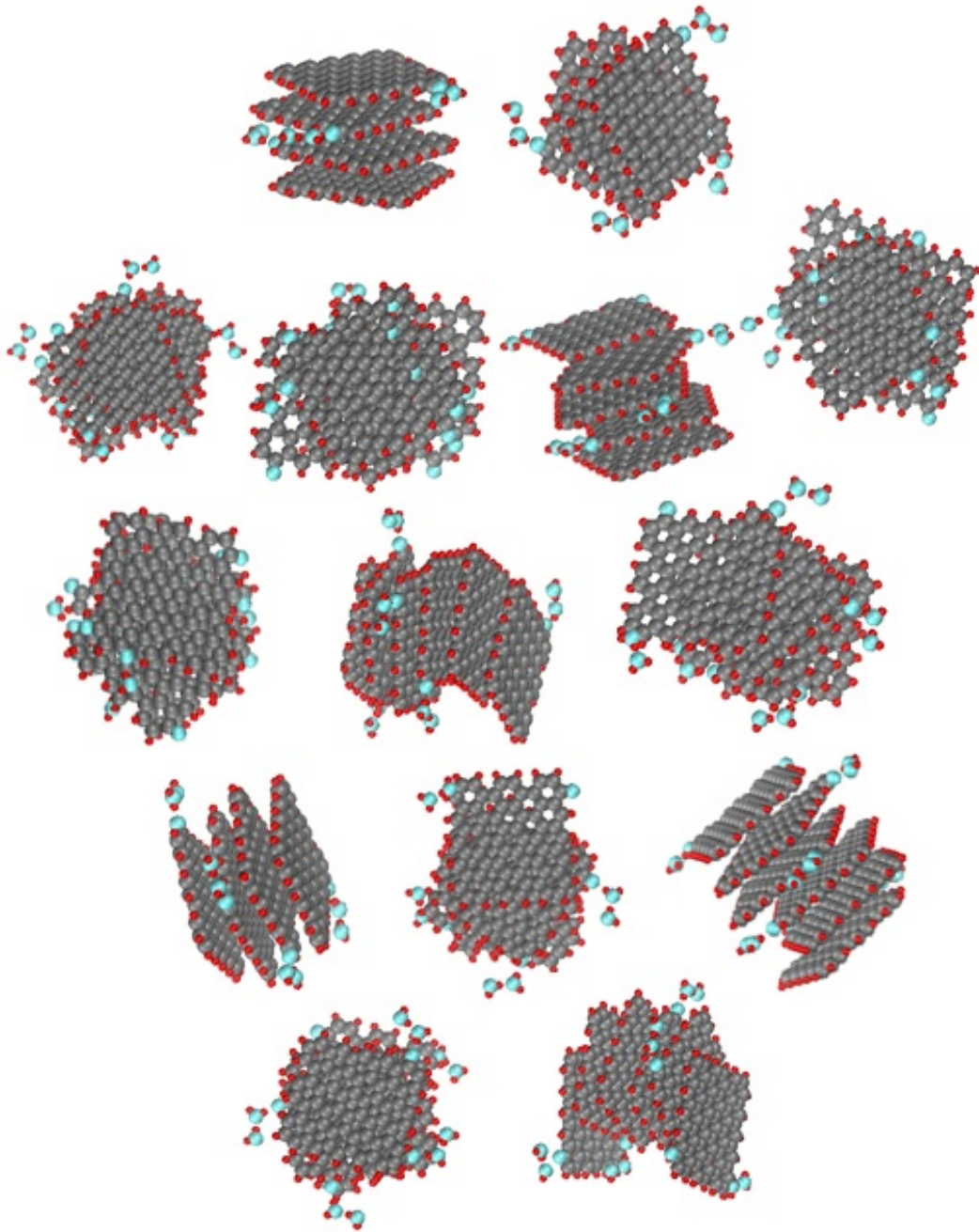


FIG. 11. Planar presentation of a model of ‘wet’ shungite globule consisting of a set of four-, five- and six-layer stacks of ‘wet’ (5, 5) rGO sheets of the  $C_{66}O_1H_{21}$  chemical composition voluntarily located and oriented in space. Linear dimensions along the vertical and horizontal are of  $\sim 6$  nm. The atom marking see in the caption to Fig.9

## 8. Conclusion

The performed neutron scattering study allows putting certain ends in the study of the structure and chemical composition of shungite. The rGO nature of the basic structural element, its size and chemical composition as well as four-six-layer stacking have received an experimental confirmation fully supporting the general concept on the shungite structure suggested earlier [3]. Both the linear size of individual rGO sheets and the sheet stacks are responsible for the obtained  $L_{CSR}$  values of 2–3 nm and 1.5–2 nm, respectively. The former characterizes not only the lateral dimension of the rGO sheets but the presence of both translational and rotational disorder (turbostratic structure) of the stack layers, the latter concerns stacks' thickness. The stacks of such dimension form globules of ~6–8 nm in size (the third level of structure) while the latter produce agglomerates of 20 nm and more (the fourth level of structure) completing the fractal packing of shungite. The basic rGO fragments are hard reduced products, actually, only slightly oxygenated graphene hydrides, of an averaged stable chemical composition described by ~6:0.1:2 (C:O:H) atom content ratio. The sheet planarity, drastically distorted for the pristine GOs (see Fig. 7a), is fully restored thus allowing to speak about 'flat graphene', or technical graphene, that is a highly important raw material for the modern graphene technologies and the natural pantry of which is presented by shungite deposits of Karelia.

## Acknowledgement

The authors greatly appreciate financial support of RSF grants 14-08-91376 (E. Sh.) and 13-03-00422 (N.R.) as well as the Basic Research Program, RAS, Earth Sciences Section-5. The grants of the Polish Plenipotentiary in JINR for the modernization project of the NERA spectrometer in 2007–2012 are gratefully acknowledged.

## References

- [1] Luo J., Kim J., Huang J. Material processing of chemically modified graphene: Some challenges and solutions. *J. Acc Chem. Res.*, **46**, P. 2225–2234 (2013).
- [2] Chua C.K., Pumera M. Chemical reduction of graphene oxide: a synthetic chemistry viewpoint. *Chem. Soc. Rev.*, **43**, P. 291–312 (2014).
- [3] Sheka E.F., Rozhkova N.N. Shungite as the natural pantry of nanoscale reduced graphene oxide *Int. J. Smart Nano Mat.*, **5**, P. 1–16 (2014).
- [4] Rozhkova N.N. Shungite Nanocarbon (in Russ). Karelian Research Centre of RAS, Petrozavodsk (2011).
- [5] Rozhkova N.N. Aggregation and stabilization of shungite carbon nanoparticles. *Russ J Gen Chem*, **83**, P. 2676–2685 (2013).
- [6] Razbirin B.S., Rozhkova N.N., Sheka E.F., et. al. Fractals of graphene quantum dots in photoluminescence of shungite. *J. Exp.Theor. Phys.*, **118**, P. 735–746 (2014).
- [7] Razbirin B.S., Rozhkova N.N., Sheka E.F. Photonics of shungite quantum dots arXiv:1406.1703v1 [cond-mat.mtrl-sci] (2014).
- [8] Li L., Wu G., Yang G., Peng J., Zhao, Zhu J.J. Focusing on luminescent graphene quantum dots: current status and future perspectives. *Nanoscale*, **5**, P. 4015–4039 (2013).
- [9] Sheka E.F., Natkaniec I., Rozhkova N.N., HoldernaNatkaniec K. Neutron scattering study of reduced graphene oxide of natural origin. *JETP Lett.*, **118**, P. 735–746 (2014).
- [10] Rozhkova N.N., Griбанov A.V., Khodorkovskii M.A. Water mediated modification of structure and physical chemical properties of nanocarbons. *Diam. Rel. Mat.*, **16**, P. 2104–2108 (2007).
- [11] Natkaniec I., Bragin S.I., Brankowski J., Mayer J. NERA spectrometer at IBR2 in Proc ICANS XII Meeting, Abington 1993, RAL Report 94-025 I: 89–85 (1994).
- [12] Opalev S.V., Belenkov E.A. Experimental study of changing graphite structure under milling. (in Russ.) *Izvestiya Chelyabinskogo Nauchnogo Centra*, **3**, P. 27–30 (2004).

- [13] Emel'yanova G.I., Gorlenko L.E., Rozhkova N.N. et. al. Effect of the conditions of structure formation on the physicochemical properties of ozonated shungites. *Russ. J. Phys. Chem. A*, **84**, P. 1376–1381 (2010).
- [14] Kovalevski V.V., Buseck P.R., Cowley J.M. Comparison of carbon in shungite rocks to other natural carbons: An X-ray and TEM study *Carbon*, **39**, P. 243–256 (2001).
- [15] Bokhenkov E.L., Natkaniec I., Sheka E.F. Determination of the density of phonon states of naphthalene crystal from inelastic incoherent neutron scattering. *J. Exp. Theor. Phys.*, **43**, P. 536–545 (1976).
- [16] Hall P.G., Pidduck A., Wright C.J. Inelastic neutron scattering by water adsorbed on silica. *J. Colloid. Interface Sci.*, **79**, P. 339–344 (1981).
- [17] Sheka E.F., Khavryutchenko V.D., Markichev I.V. Technological polymorphism of disperse amorphous silicas: inelastic neutron scattering and computer modeling *Russ. Chem. Rev.*, **64**, P. 389–414 (1995).
- [18] Crupi V., Majolino D., Migliardo P., Venuti V. Neutron scattering study and dynamic properties of hydrogen-bonded liquids in mesoscopic confinement. 1. The water case. *J. Phys. Chem. B*, **106**, P. 10884–10894 (2002).
- [19] Buchsteiner A., Lerf A., Pieper J. Water dynamics in graphite oxide investigated with neutron scattering. *J. Phys. Chem. B*, **110**, P. 22328–22338 (2006).
- [20] Corsaro C., Crupi V., Majolino D. et. al. Inelastic neutron scattering study of water in hydrated LTA-type zeolites. *J. Phys. Chem. A*, **110**, P. 1190–1195 (2006).
- [21] Natkaniec I., Sheka E.F., Drubicki K. et. al. arXiv:1411.xxxx [cond-mat.mtrl-sci] (2014).
- [22] Bertrand C.E., Zhang Y., Chen S.H. Deeply-cooled water under strong confinement: neutron scattering investigations and the liquid–liquid critical point hypothesis. *Phys. Chem. Chem. Phys.*, **15**, P. 721–745 (2013).
- [23] Avdeev M.V., Tropin T.V., Aksenov V.L. et. al. Pore structures in shungites as revealed by small-angle neutron scattering *Carbon*. **44**, P. 954–961 (2006).
- [24] Sheka E.F., Popova N.A. Molecular theory of graphene oxide. *Phys. Chem. Chem. Phys.*, **15**, P. 13304–13322 (2013).
- [25] Golubev E.A. Private communication.
- [26] Druzicki K., Natkaniec I. Vibrational properties of water retained in graphene oxide. *Chem. Phys. Lett.*, **600**, P. 106–111 (2014).
- [27] Sheka E.F. Computational strategy for graphene: Insight from odd electrons correlation *Int. J. Quant. Chem.*, **112**, P. 3076–3090 (2012).
- [28] Xu Z., Bando Y., Liu L. et. al. Electrical conductivity, chemistry, and bonding alternations under graphene oxide to graphene transition as revealed by *in situ TEM*. *ACS Nano*, **5**, P. 4401–4406 (2011).
- [29] Tkachev S.V., Buslaeva E.Yu., Naumkin A.V. et. al. Reduced graphene oxide *Inorg. Mater.*, **48**, P. 796–802 (2011).
- [30] Stobinski L. [www.nanomaterials.pl](http://www.nanomaterials.pl) (2014).
- [31] Sheka E.F., Popova N.A. Odd-electron molecular theory of the graphene hydrogenation. *J. Mol. Mod.*, **18**, P. 3751–3768 (2012).